

# Coherent Lattice Vibrations in Mono- and Few-Layer WSe<sub>2</sub>

Tae Young Jeong,<sup>†,‡</sup> Byung Moon Jin,<sup>†</sup> Sonny H. Rhim,<sup>§</sup> Lamjed Debbichi,<sup>||</sup> Jaesung Park,<sup>‡</sup> Yu Dong Jang,<sup>†</sup> Hyang Rok Lee,<sup>†</sup> Dong-Hun Chae,<sup>‡</sup> Donghan Lee,<sup>†</sup> Yong-Hoon Kim,<sup>||</sup> Suyong Jung,<sup>‡</sup> and Ki Ju Yee<sup>\*,†</sup>

<sup>†</sup>Department of Physics, Chungnam National University, Daejeon 305-764, Republic of Korea

<sup>‡</sup>Korea Research Institute of Standards and Science, Daejeon 305-340, Republic of Korea

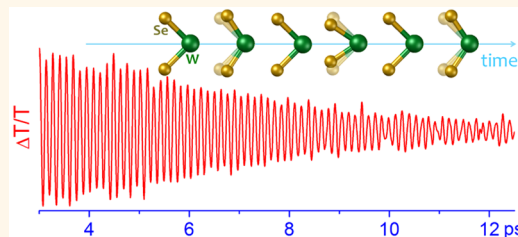
<sup>§</sup>Department of Physics and Energy Harvest Storage Research Center, University of Ulsan, Ulsan 680-749, Republic of Korea

<sup>||</sup>Graduate School of Energy, Environment, Water, and Sustainability, Korea Advanced Institute of Science and Technology, Daejeon 305-701, Republic of Korea

## S Supporting Information

**ABSTRACT:** We report the observation of coherent lattice vibrations in mono- and few-layer WSe<sub>2</sub> in the time domain, which were obtained by performing time-resolved transmission measurements. Upon the excitation of ultrashort pulses with the energy resonant to that of A excitons, coherent oscillations of the A<sub>1g</sub> optical phonon and longitudinal acoustic phonon at the M point of the Brillouin zone (LA(M)) were impulsively generated in monolayer WSe<sub>2</sub>. In multilayer WSe<sub>2</sub> flakes, the interlayer breathing mode (B<sub>1</sub>) is found to be sensitive to the number of layers, demonstrating its usefulness in characterizing layered transition metal dichalcogenide materials. On the basis of temperature-dependent measurements, we find that the A<sub>1g</sub> optical phonon mode decays into two acoustic phonons through the anharmonic decay process.

**KEYWORDS:** transition metal dichalcogenides, WSe<sub>2</sub>, coherent lattice vibration, monolayer, anharmonic decay



Layered semiconducting transition metal dichalcogenides (TMDCs) such as MoS<sub>2</sub>, MoSe<sub>2</sub>, WS<sub>2</sub>, and WSe<sub>2</sub> have attracted great interest because of their unique optical and electrical properties.<sup>1–9</sup> Transition metal atoms (Mo or W) are covalently bonded to chalcogenide atoms (S or Se) to form an individual layer, and van der Waals interactions cause each layer to stack into multilayered films. Notably, semiconducting TMDCs exhibit evolutionary behaviors with the number of layers, especially in terms of their optical properties. Being an indirect band-gap semiconductor in bulk crystals, for example, the energy of the indirect gap widens as the number of layers decreases while the size of the direct band gap is maintained, causing a transition to a direct-band gap semiconductor in a monolayer form. Accordingly, the strong photoluminescence (PL) observed in the monolayer is quenched in multilayer films,<sup>1,3,10</sup> although direct-band gap behaviors can be restored in multilayers by applying external strains.<sup>11</sup> The frequency of the Raman modes also varies with the layer thickness, which makes Raman spectroscopy a general method to verify the layer number of semiconducting TMDCs<sup>12–18</sup> as in the case of graphene.

Phonons, the fundamental vibrational modes of a crystal lattice, play important roles in determining many physical properties of 2D materials. For example, thermal conductivity is determined by the dynamics of lattice motions and excited

carriers cool down to band edges by releasing the excess energy *via* optical or acoustic phonons. Electrical conductivity is also affected by electron scatterings with optical phonons, thus limiting the mobility of TMDC materials.<sup>19</sup> By studying light scatterings with phonons near electronic transition energies, resonant Raman spectroscopy has been quite effective in the characterization of TMDC materials. For example, resonance profiles were studied and the harmonics or combinations of zone-edge phonons were detected from Raman scatterings near exciton energies.<sup>18,20–25</sup>

Despite substantial progress in the investigation of phonons using continuous-wave Raman scattering, real-time observation of coherent lattice vibration modes in mono- and few-layer TMDCs has yet to be reported. By monitoring coherent phonons in real time, it is possible to visualize the lattice motions in the time domain and investigate the phonon decay process as well as the oscillation phase, providing complementary information that is not accessible with Raman measurements.<sup>26–29</sup> Furthermore, even for resonant excitations where fluorescence photons overwhelm phonon signals in

Received: April 3, 2016

Accepted: April 20, 2016

Published: April 22, 2016

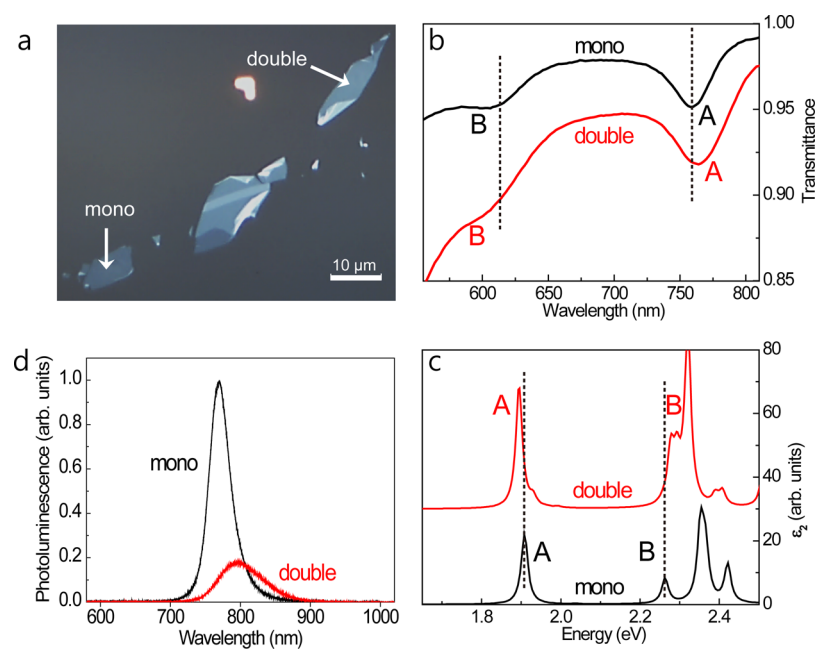


**Figure 1.** (a) Optical microscope image showing mono- and double-layer  $\text{WSe}_2$  flakes. (b) Transmission spectra, (c) calculated spectra for the excitonic optical absorption, and (d) PL spectra of mono- and double-layer  $\text{WSe}_2$ .

Raman scatterings, it is possible to detect coherent phonons by measuring the transmission change of the probe beam.

Monolayer  $\text{WSe}_2$  has 9 normal phonon modes with the  $D_{3h}$  symmetry, whereas bulk  $\text{WSe}_2$ , belonging to the point group  $D_{6h}$  has 18 vibration modes. Among those, the  $E_{2g}^1$  and  $A_{1g}$  modes are common Raman-active lattice vibrations from both mono- and multilayer  $\text{WSe}_2$ . In the  $E_{2g}^1$  mode, W and Se atoms move in opposite directions within the layer plane. In contrast, two Se atoms surrounding a W atom make out-of-plane displacements in the  $A_{1g}$  mode. Because the  $A_{1g}$  mode becomes hardened and the  $E_{2g}^1$  mode softened as the layer number increases, the frequency difference of these two phonon modes was used to determine the layer thickness of TMDC films.<sup>12,13,16</sup> Additionally, the interlayer breathing ( $B_1$ ) and shear (S) modes are also Raman active and sensitive to the layer thickness.<sup>15,17</sup>

In this work, we report the observation of coherent lattice vibrations in mono- and few-layer  $\text{WSe}_2$ . Using ultrafast time-resolved transmission measurements, we observe the atomic motions of the out-of-plane  $A_{1g}$  and the interlayer  $B_1$  modes in the time domain. The pump photons, whose energy closely tuned to that of the A exciton in  $\text{WSe}_2$ , generate non-equilibrium exciton population and coherent lattice vibrations, and their evolutions with time are monitored using time-delayed probe photons. We investigate resonance behaviors of the lattice vibrations near the A exciton and present the evolution of the phonon modes with the layer number. Moreover, temperature-dependent measurements in multilayer  $\text{WSe}_2$  indicate that the  $A_{1g}$  optical phonon actively decays into two acoustic modes through the anharmonic decay process.

## RESULTS AND DISCUSSION

As displayed in the optical image of Figure 1a,  $\text{WSe}_2$  flakes exhibit different optical contrasts depending on the number of layers. To obtain few-layer  $\text{WSe}_2$ , we first mechanically exfoliate the bulk crystals and transfer the few-layer flakes onto double-layer polymer films. After identifying the number of layers with

Raman and PL measurements, we transfer the flakes onto transparent quartz substrates for transmission measurements. With this method, we routinely obtain thin  $\text{WSe}_2$  flakes with a typical size of  $\sim 100 \mu\text{m}^2$  (see Methods). Figure 1b shows the transmission spectra from both the mono- and double-layer  $\text{WSe}_2$  flakes. The absorption peaks located at  $\sim 760$  and  $\sim 600$  nm correspond to the optical transitions of the A and B excitons, respectively. These excitonic peaks originate from the direct-gap transitions at the K points between the valence bands that have been spin split due to the strong spin–orbit coupling and the conduction band.<sup>10,30</sup> Although they are not clearly resolved at room temperature, the well-defined signals of A and B excitons appear in the transmissions measured at 80 K (see Supporting Information). The A and B excitonic peaks, which have been blue-shifted from their room-temperature positions,<sup>31</sup> exhibit a slightly increased energy difference in the double-layer  $\text{WSe}_2$  (0.46 eV) compared with the monolayer case (0.43 eV). To clarify the origin of this behavior, we have calculated the optical absorption spectra of monolayer and bilayer  $\text{WSe}_2$  based on the many-body GW plus Bethe–Salpeter equation (BSE) formalism. The GW–BSE spectra shown in Figure 1c reproduce the experimentally observed slight downshift of the A exciton peak in the  $\text{WSe}_2$  bilayer,<sup>10</sup> which results from the enhanced splitting of the valence band maximum at the K point in the double-layer.<sup>30</sup> This is again caused by the interlayer interaction and reduced quantum confinement effect in the double-layer, which can be more clearly seen by comparing the first excitonic peaks obtained without spin–orbit coupling (before the A–B splitting) in the monolayer and the double-layer (see Supporting Information). In agreement with earlier studies,<sup>1,3,10</sup> the PL spectra shown in Figure 1d exhibit much stronger PL signal from the monolayer than the double layer, which is attributed to the direct-to-indirect band gap transition. For the monolayer, the PL peak ( $\sim 766$  nm) is Stokes shifted by 7 nm from the absorption peak of the A exciton ( $\sim 760$  nm). Hence, resonant features relevant to the A exciton are expected to play a significant role in the

time-resolved pump–probe measurements when 750 nm (1.65 eV) photons are used.

Figure 2a presents a schematic of the time-resolved pump probe experiments using ultrashort pulses with a center

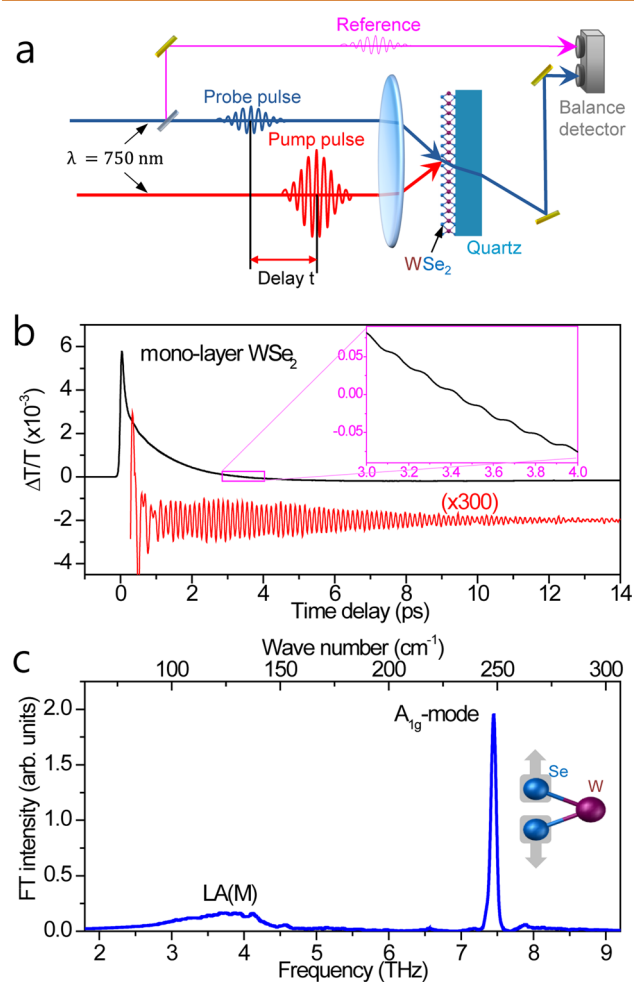


**Figure 2.** (a) Schematic experimental setup of pump–probe measurements. (b) Photoinduced change of the probe transmission as a function of the time delay relative to the pump pulse obtained for the monolayer WSe<sub>2</sub> with ultrashort pulses with a center wavelength of 750 nm. The inset is an expanded plot visualizing high-frequency modulations superimposed with the signal. The red curve is the oscillatory part of the signal, which was extracted by subtracting the slowly varying component from the signal. (c) FT spectrum of the time-domain lattice vibrations showing the out-of-plane A<sub>1g</sub> mode at 7.448 THz and the broad peak at approximately 3.7 THz due to the LA(M) mode.

wavelength of 750 nm. We implement the balanced detection using a reference beam in order to improve the signal-to-noise ratio. The pump pulse induces nonequilibrium excitons and lattice vibrations in WSe<sub>2</sub>, and the resultant optical changes are monitored by detecting the transmitted probe beam as a function of the time delay between the pump and probe pulse. Previous time-resolved pump–probe experiments on WSe<sub>2</sub> have revealed the dynamics of photoexcited excitons such as the recombination, diffusion, and intervalley scattering processes.<sup>9,32–36</sup> The impulsive ultrashort pulses can also macroscopically launch the coherent motion of lattice vibrations, which in turn modulate optical constants of the material. Then, the temporal motion of lattice vibrations can be

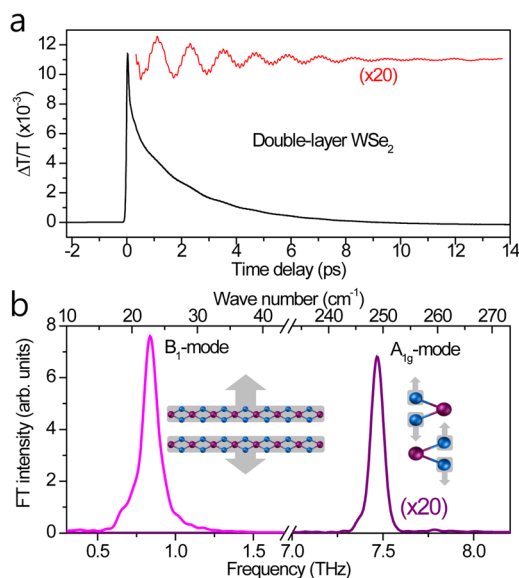
visualized with monitoring the probe pulse in ultrafast pump–probe experiments.

Figure 2b shows the time-resolved transmission change ( $\Delta T$ ) of the probe pulse through the monolayer WSe<sub>2</sub>. With the generation of A excitons by the pump pulse, the absorption probability of the probe beam decreases because excited states are inactive to optical transitions, which explains the onset of the positive transmission change at zero time delay. The background  $\Delta T$  signal of the monolayer WSe<sub>2</sub> is fitted well by a biexponential decay function, with two decay constants of  $\tau_1 = 0.08$  ps and  $\tau_2 = 1.2$  ps, for the fast and slow processes, respectively. The slow part corresponds to the decay of the A exciton through the radiative or nonradiative recombinations. The fast process is not clearly resolved with the 60 fs pulse duration in this work, but it is probably related with ultrafast dephasing.<sup>9,37</sup>

Because of the electron–phonon coupling, the equilibrium position of the lattice depends on the exciton population and undergoes an abrupt shift with the pump pulse. Then, with a finite response time, the motion of the lattice initiates damped harmonic oscillations around the new equilibrium position. This kind of coherent phonon generation is referred to as the displacive excitation mechanism.<sup>28</sup> As is evident from the expanded plot of the inset, the high-frequency modulations from the lattice are superimposed with the electronic contributions. We extract pure oscillatory components by subtracting the monotonously decaying electronic contributions of  $\Delta T$ . The resultant high-frequency modulations are from the coherent lattice vibrations in the monolayer WSe<sub>2</sub> flake (red curve in Figure 2b).

The frequencies of lattice vibrations are clarified from Fourier transform (FT) of the time domain signal. The FT spectrum of the oscillatory  $\Delta T$  in Figure 2b is shown in Figure 2c, revealing that a couple of strong lattice modes exist: one of which has a central frequency of 7.448 THz (248.3 cm<sup>-1</sup>) and the other exhibits a rather broad peak near 3.7 THz (123 cm<sup>-1</sup>). Here, we assign the strong peak at 7.448 THz to the A<sub>1g</sub> optical phonon and the peak at 3.7 THz to the LA(M) mode.<sup>18,38</sup> We note that in resonant Raman scattering of TMDC materials, although the harmonics or combined phonon modes relevant to the LA(M) have been widely reported, the first-order LA(M) mode was not observed or very weak owing to the momentum mismatch of the scattering mechanism. The A<sub>1g</sub> phonons in the monolayer WSe<sub>2</sub> has a dephasing time of 4.5 ps, which was inferred from the fitting of temporal oscillations with an exponentially decaying sinusoidal function (see Supporting Information for the fitting procedure). Interestingly, the contributions from the E<sub>2g</sub> phonons are negligible, even though their strength is comparable to that of the A<sub>1g</sub> phonons in Raman scattering spectra.<sup>16</sup> Although further investigations are required, we attribute the predominant A<sub>1g</sub> phonon signal in the transmission change to the sensitive modulation of the A exciton resonance by the out-of-plane A<sub>1g</sub> lattice motion.

For the double-layer WSe<sub>2</sub>, time-resolved transmission change (black curve) and extracted oscillatory signal (red curve) are displayed in Figure 3a, and the FT spectrum of the lattice vibrations is presented in Figure 3b. Similarly to the monolayer WSe<sub>2</sub>, we can assign the peak at 7.482 THz to the A<sub>1g</sub> optical phonon at the  $\Gamma$  point. Among noticeable differences, however, are the missing LA(M) phonon mode in the double-layer spectrum. Instead, a strong peak is observed at 0.838 THz, which corresponds to the interlayer breathing



**Figure 3.** (a) Photoinduced transmission changes obtained for the double-layer WSe<sub>2</sub> flake, with the red curve representing the oscillatory part extracted from the signal. (b) Fourier-transformed spectrum of the time-domain oscillations showing the interlayer breathing (B<sub>1</sub>) mode at 0.838 THz and the A<sub>1g</sub> mode at 7.482 THz.

mode (B<sub>1</sub>). In order for the LA(M) phonons to activate, inelastic scattering events at structural defects or along the edges are necessary to compensate for the wave vector mismatch between phonons and photons, which may be easier under the A exciton resonance. Note that the defect-induced D-mode is generally more distinctive in monolayer graphene than in multilayer graphene<sup>39,40</sup> because the scatterings along the edges are expected to be stronger for monolayer films.

It is expected that multilayered TMDCs have interlayer phonon modes that are assorted into out-of-plane breathing (B) and in-plane shear (S) modes. Zhao et al. demonstrated from the low-energy Raman scattering measurements that the B-mode (S-mode) becomes softened (hardened) as the number of layers increases.<sup>17</sup> The absence of the in-plane S-mode in our data is consistent with the selectivity of the optical modes in the sense that the time-resolved transmissivity measurement is exclusively sensitive to out-of-plane atomic motions in layered TMDC materials. We observe that the dephasing times of the B<sub>1</sub> and A<sub>1g</sub> phonons are  $\tau_{B_1} = 3.5$  ps and  $\tau_{A_{1g}} = 4.3$  ps, respectively, for the double-layer WSe<sub>2</sub>.

The interlayer breathing mode is highly sensitive to the layer thickness. Figure 4a displays the oscillatory signals of the B<sub>1</sub> mode from double-, triple-, and quadruple-layer WSe<sub>2</sub>, and the corresponding FT spectra are plotted in Figure 4b. Figure 4c shows the layer-number dependence of the A<sub>1g</sub> mode, and Figure 4d summarizes the frequency shifts of the A<sub>1g</sub>- and B<sub>1</sub>-mode oscillations with the layer number. It is consistent with previous Raman measurements that the frequency of the B<sub>1</sub> mode decreases as the layer number increases. Note that the shift of the B<sub>1</sub> mode can be used as a robust layer-number characterization tool because of its high fidelity (Figure 4b) compared with the gradual evolution of the A<sub>1g</sub> phonons (Figure 4c). In addition, we also find that the dephasing time of the B<sub>1</sub> mode is dependent on the layer number. For the quadruple-layer WSe<sub>2</sub>, the dephasing time  $\tau_{B_1} = 5.4$  ps is longer than the cases of triple-layer (3.8 ps) and double-layer (3.5 ps) flakes. Rough estimation suggests that the dephasing time has a

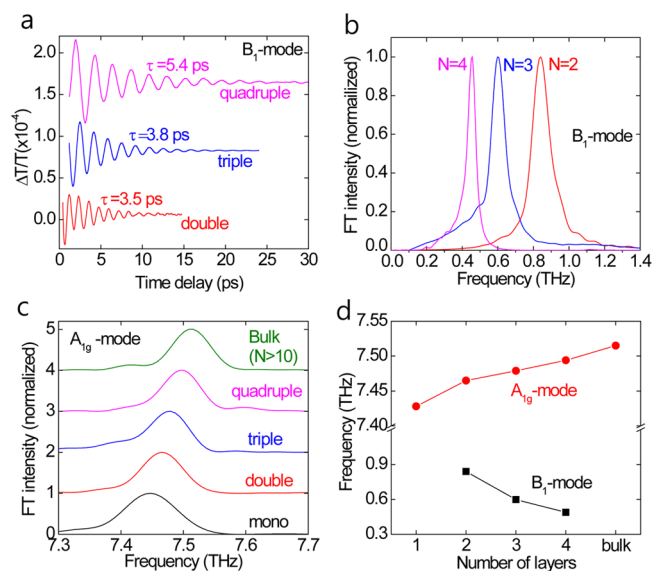


**Figure 4.** (a) Time-domain transmission oscillations of the B<sub>1</sub> mode and (b) corresponding FT spectra for the double-, triple-, and quadruple-layer WSe<sub>2</sub> flakes. (c) Fourier-transformed spectra of the out-of-plane A<sub>1g</sub> mode for few-layer WSe<sub>2</sub> flakes. (d) Frequency of the B<sub>1</sub> and A<sub>1g</sub> modes as a function of the layer number.

tendency to scale with the period of lattice vibrations (inverse of phonon frequency). Here, we note that Ge et al. have observed similar results on relatively thick MoS<sub>2</sub> flakes with the layer number  $N > 10$ , that the period (frequency) of the coherent LA phonon oscillations increases (decreases) as the decay time becomes longer in thicker MoS<sub>2</sub>.<sup>41</sup>

Further information on the dephasing process of the A<sub>1g</sub> mode can be obtained from temperature-dependent measurements. Figure 5a shows the A<sub>1g</sub> phonon oscillations of a bulk WSe<sub>2</sub> film (>10 layers) at different temperatures. The frequency shifts and dephasing rates of the A<sub>1g</sub> optical phonons are presented in Figure 5b and c, respectively, for the bulk (purple) and quadruple-layer (blue) WSe<sub>2</sub>. It is well known that an optical phonon can split into two phonons with lower frequencies, conserving the energy and momentum. In this anharmonic phonon dephasing process, the dephasing rate ( $\Gamma_{A_{1g}}$ ) and frequency ( $\Omega_{A_{1g}}$ ) are a function of temperature ( $T$ ) and is described by<sup>42</sup>

$$\Gamma_{A_{1g}} = \Gamma_0 + \Gamma_{anh} \times [1 + n(E_1) + n(E_2)]$$

$$\Omega_{A_{1g}} = \Omega_0 + A \times [1 + n(E_1) + n(E_2)] \quad (1)$$

Here,  $n(E_{1,2}) = [\exp(E_{1,2}/k_B T) - 1]^{-1}$  is the thermal occupation number of the lower frequency phonons with energy  $E_1$  or  $E_2$ , and  $k_B$  is the Boltzmann constant.  $\Gamma_{anh}$  and  $A$  are the proportional constants, and  $\Gamma_0$  and  $\Omega_0$  are background contributions to the dephasing rate and frequency, respectively. The solid lines in Figure 5b and c are numerical fittings obtained using eq 1 with  $E_1 = E_2 = \hbar\Omega_{A_{1g}}/2$ , considering the anharmonic process in which one A<sub>1g</sub> phonon decays into two lower-frequency phonons with the same frequency but opposite wave vectors. As shown in Figure 2, a considerable density of the LA modes exists at the M point of the Brillouin zone with a frequency near  $\Omega_{A_{1g}}/2$  ( $\sim 3.7$  THz),<sup>14</sup> suggesting that large portion of A<sub>1g</sub> phonons in WSe<sub>2</sub> can decay into two LA(M) phonons through the anharmonic process (see Supporting

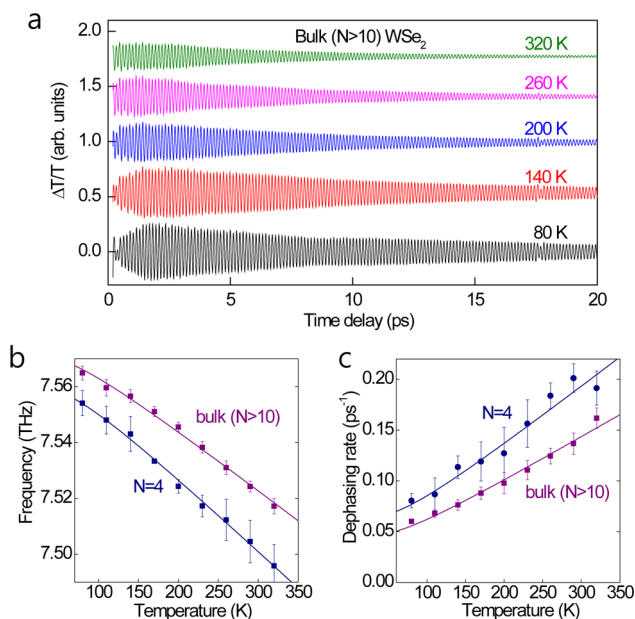


**Figure 5.** (a) Coherent lattice vibrations of the  $A_{1g}$  mode for bulk  $WSe_2$  obtained at different temperatures ranging from 80 to 320 K. (b) Frequency and (c) dephasing rate of the  $A_{1g}$  mode as a function of temperature for the quadruple-layer and bulk  $WSe_2$  flakes. The filled scatter points are experimental data, and the solid lines are fitting curves of the anharmonic decay model.

Information for the contribution of carrier-phonon interactions).

When the applied photon energy is tuned to match the transition energy of a specimen, optoelectronic signals can be enhanced in various ways. In pump–probe experiments, resonance effects can be induced in the excitation process by pump photons as well as in the detection stage by probe photons. Figure 6a shows the FT intensity of the  $A_{1g}$  phonon mode from the monolayer  $WSe_2$  obtained with varying the center wavelength of pump and probe photons. The PL spectrum is also displayed for comparison. The detection efficiency of the  $A_{1g}$  mode oscillation is maximum at  $\lambda_c \approx 740$  nm. Assuming that the absorption profile changes in

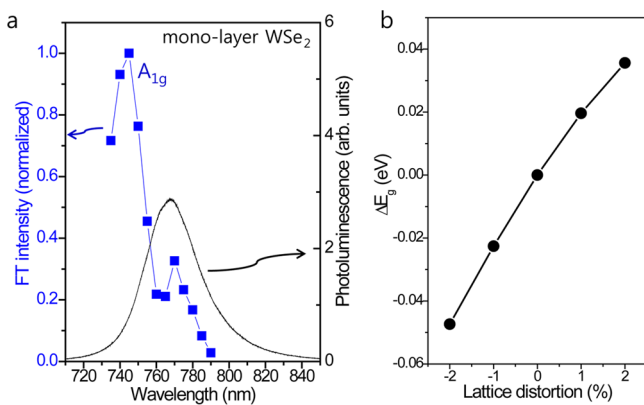


**Figure 6.** (a) Fourier-transformed intensity of the  $A_{1g}$  phonon oscillations of monolayer  $WSe_2$  flake as a function of the center wavelength of ultrashort pulses. The PL spectrum of the same flake is displayed for comparison. (b) Density-functional calculation of the energy gap shift at the K point of the Brillouin zone as a function of the lattice distortion of the  $A_{1g}$  mode.

accordance with the atomic coordinates of the  $A_{1g}$  phonon mode, the detection efficiency will be proportional to the energy derivative of the resonance profile, which can explain the reason why the strongest  $A_{1g}$  mode is detected at the high-energy shoulder of the PL peak rather than at the peak of the PL spectrum. The density-functional calculation suggests that the energy bands are modulated according to lattice distortions accompanied by the  $A_{1g}$  mode. Once influenced by the lattice distortion, valleys in the conduction and valence bands at the K point move upward or downward depending on the distortion polarity (see Supporting Information). In the calculation, change of the bands was found to be more susceptible to the displacement of the  $A_{1g}$  mode than that of the  $E_{2g}^1$  mode, being consistent with not observing coherent  $E_{2g}^1$  oscillations from the transmission change. The unbalanced features of  $A_{1g}$  phonon intensity around the exciton resonance can be attributed to the asymmetry in the generation efficiency, which could be further confirmed by performing nondegenerate pump–probe measurements with tuning the pump and probe energies independently.

## CONCLUSION

By performing pump–probe experiments with ultrashort pulses resonant with the A exciton of the mono- and few-layer  $WSe_2$ , we were able to visualize coherent lattice vibration modes in the time domain, especially out-of-plane motions of the intralayer  $A_{1g}$  mode and the interlayer breathing mode  $B_1$ . Dephasing time of the  $A_{1g}$  mode was found to be around 4.5 ps for the monolayer  $WSe_2$ . From temperature-dependent measurements of the  $A_{1g}$  phonons in multilayer  $WSe_2$ , the accelerated phonon dephasing with temperature was modeled by the anharmonic process, in which the  $A_{1g}$  mode decays into two acoustic modes of LA(M). The frequency of the interlayer breathing mode ( $B_1$ ), being strongly dependent on the number of layers, has proven to be a powerful characterization method of the layer thickness of TMDCs. The observed phonon dynamics in this study will be useful in predicting the performance of TMDC-based devices as well as in understanding their physical properties.

## METHODS

**Sample Preparation.** Transparent samples were obtained by transferring  $WSe_2$  flakes onto quartz substrates. First, using the scotch tape method,  $WSe_2$  flakes were mechanically exfoliated from bulk crystals onto silicon wafers covered by double polymer layers consisting of a water-soluble layer (PSS; poly(4-styrenesulfonic acid)) and PMMA, in which the PSS/PMMA thickness was carefully selected to better classify monolayers by optical contrast. Then, an OHP frame with a square hole was attached to the layer with the  $WSe_2$  flakes located inside the hole. By dissolving the PSS layer in deionized water, we obtained the OHP/PMMA membrane with  $WSe_2$  flakes, which was then transferred onto a quartz substrate. Finally, we removed the PMMA layer in acetone.

**Pump–Probe Experiment.** Photoinduced change of the time-resolved transmission was measured by performing pump–probe experiments using a cavity-dumped Ti:sapphire laser, which delivers ultrashort pulses with a duration of approximately 60 fs at a repetition rate of 400 kHz. The center wavelength was tuned around 750 nm. A beam splitter divides the beam with a ratio of 4:1 for the strong pump and weak probe. After the pump beam passes a shaking mirror in order to modulate the path length, an objective lens with a numerical aperture of 0.57 focuses the two beams at the same spot in the sample. The focused spot size was approximately  $5 \mu m$  in diameter, and a pump fluence of approximately  $1.0 \text{ mJ}/\text{cm}^2$  was used. The shaker scans the time delay between the pump and probe pulses at a frequency as

fast as 13 Hz, and the high-speed data acquisition with data averaging enabled us to obtain high-quality signals with a signal-to-noise ratio as low as  $10^{-7}$ .

**Photoluminescence and Transmission Measurement.** WSe<sub>2</sub> samples were excited by a continuous wave laser at 532 nm to measure PL using a monochromator equipped with a CCD detector. The transmission spectra were measured using a supercontinuum laser delivering broadband light in the 450–2400 nm region.

**Computational Methods.** We performed first-principles calculations with the projector-augmented wave scheme as implemented in the VASP code.<sup>43</sup> The plane-wave cutoff was set to 400 eV and the exchange correlation contributions were treated within the local density approximation as well as Perdew–Burke–Ernzerhof generalized gradient approximation augmented by empirical dispersion corrections proposed Tkatchenko–Scheffler.<sup>44</sup> The two-dimensional slabs were prepared with a vacuum space of about 15 Å along the direction normal to the WSe<sub>2</sub> plane to ensure decoupling between periodic images. A  $12 \times 12 \times 1$   $\Gamma$ -centered  $k$  points were sampled within the Brillouin zone for the band structure calculations, and an increased  $14 \times 14 \times 1$   $k$ -point mesh was used for the GW–BSE calculations. These ground-state calculations were then used to compute the quasiparticle eigenvalues within the non-self-consistent GW scheme ( $G_0W_0$ ) with and without including the spin–orbit coupling.<sup>30,45</sup> The cutoff for the response function was set to 150 eV, and more than 256 bands were included for the calculation of the polarizability and the self-energy. Using the  $G_0W_0$  quasiparticle bands, we solved the Bethe–Salpeter equation within the Tamm–Dancoff approximation to account for the interactions between quasidelectrons and quasiholes.<sup>30,46</sup> The six highest valence bands and the eight lowest conduction bands were used as a basis for the excitonic eigenstates.

## ASSOCIATED CONTENT

### Supporting Information

The Supporting Information is available free of charge on the ACS Publications website at DOI: 10.1021/acsnano.6b02253.

Pump fluence dependence, fitting procedure of the lattice vibration, density-function calculation of energy bands, transmission spectra at 80 K, and  $G_0W_0$ +BSE calculations for the excitonic optical absorption spectra. (PDF)

## AUTHOR INFORMATION

### Corresponding Author

\*E-mail: kyee@cnu.ac.kr

### Notes

The authors declare no competing financial interest.

## ACKNOWLEDGMENTS

This work was supported by the National Research Foundation of Korea (NRF) grant funded by the Korean government (2013R1A2A2A01067707) and the research fund of 2014 Chungnam National University. Y.-H.K. acknowledges the NRF Global Frontier Hybrid Interface Materials program (2013M3A6B1078881).

## REFERENCES

- (1) Mak, K. F.; Lee, C.; Hone, J.; Shan, J.; Heinz, T. F. Atomically Thin MoS<sub>2</sub>: A New Direct-Gap Semiconductor. *Phys. Rev. Lett.* **2010**, *105*, 136805.
- (2) Ramakrishna Matte, H.; Gomathi, A.; Manna, A. K.; Late, D. J.; Datta, R.; Pati, S. K.; Rao, C. MoS<sub>2</sub> and WS<sub>2</sub> Analogues of Graphene. *Angew. Chem.* **2010**, *122*, 4153–4156.
- (3) Eda, G.; Yamaguchi, H.; Voiry, D.; Fujita, T.; Chen, M.; Chhowalla, M. Photoluminescence from Chemically Exfoliated MoS<sub>2</sub>. *Nano Lett.* **2011**, *11*, 5111–5116.
- (4) Radisavljevic, B.; Radenovic, A.; Brivio, J.; Giacometti, V.; Kis, A. Single-Layer MoS<sub>2</sub> Transistors. *Nat. Nanotechnol.* **2011**, *6*, 147–150.

- (5) Yin, Z.; Li, H.; Li, H.; Jiang, L.; Shi, Y.; Sun, Y.; Lu, G.; Zhang, Q.; Chen, X.; Zhang, H. Single-Layer MoS<sub>2</sub> Phototransistors. *ACS Nano* **2012**, *6*, 74–80.

- (6) Wang, Q. H.; Kalantar-Zadeh, K.; Kis, A.; Coleman, J. N.; Strano, M. S. Electronics and Optoelectronics of Two-Dimensional Transition Metal Dichalcogenides. *Nat. Nanotechnol.* **2012**, *7*, 699–712.

- (7) Zeng, H.; Dai, J.; Yao, W.; Xiao, D.; Cui, X. Valley Polarization in MoS<sub>2</sub> Monolayers by Optical Pumping. *Nat. Nanotechnol.* **2012**, *7*, 490–493.

- (8) Zeng, H.; Liu, G.-B.; Dai, J.; Yan, Y.; Zhu, B.; He, R.; Xie, L.; Xu, S.; Chen, X.; Yao, W.; Cui, X. Optical Signature of Symmetry Variations and Spin-Valley Coupling in Atomically Thin Tungsten Dichalcogenides. *Sci. Rep.* **2013**, *3*, 1608.

- (9) Kim, J.; Hong, X.; Jin, C.; Shi, S.-F.; Chang, C.-Y. S.; Chiu, M.-H.; Li, L.-J.; Wang, F. Ultrafast Generation of Pseudo-Magnetic Field for Valley Excitons in WSe<sub>2</sub> Monolayers. *Science* **2014**, *346*, 1205–1208.

- (10) Zhao, W.; Ghorannevis, Z.; Chu, L.; Toh, M.; Kloc, C.; Tan, P.-H.; Eda, G. Evolution of Electronic Structure in Atomically Thin Sheets of WS<sub>2</sub> and WSe<sub>2</sub>. *ACS Nano* **2013**, *7*, 791–797.

- (11) Desai, S. B.; Seol, G.; Kang, J. S.; Fang, H.; Battaglia, C.; Kapadia, R.; Ager, J. W.; Guo, J.; Javey, A. Strain-Induced Indirect to Direct Bandgap Transition in Multilayer WSe<sub>2</sub>. *Nano Lett.* **2014**, *14*, 4592–4597.

- (12) Lee, C.; Yan, H.; Brus, L. E.; Heinz, T. F.; Hone, J.; Ryu, S. Anomalous Lattice Vibrations of Single- and Few-Layer MoS<sub>2</sub>. *ACS Nano* **2010**, *4*, 2695–2700.

- (13) Li, H.; Zhang, Q.; Yap, C. C. R.; Tay, B. K.; Edwin, T. H. T.; Olivier, A.; Baillargeat, D. From Bulk to Monolayer MoS<sub>2</sub>: Evolution of Raman Scattering. *Adv. Funct. Mater.* **2012**, *22*, 1385–1390.

- (14) Sahin, H.; Tongay, S.; Horzum, S.; Fan, W.; Zhou, J.; Li, J.; Wu, J.; Peeters, F. Anomalous Raman Spectra and Thickness-Dependent Electronic Properties of WSe<sub>2</sub>. *Phys. Rev. B: Condens. Matter Mater. Phys.* **2013**, *87*, 165409.

- (15) Zhang, X.; Han, W.; Wu, J.; Milana, S.; Lu, Y.; Li, Q.; Ferrari, A.; Tan, P. Raman Spectroscopy of Shear and Layer Breathing Modes in Multilayer MoS<sub>2</sub>. *Phys. Rev. B: Condens. Matter Mater. Phys.* **2013**, *87*, 115413.

- (16) Zhao, W.; Ghorannevis, Z.; Amara, K. K.; Pang, J. R.; Toh, M.; Zhang, X.; Kloc, C.; Tan, P. H.; Eda, G. Lattice Dynamics in Mono- and Few-Layer Sheets of WS<sub>2</sub> and WSe<sub>2</sub>. *Nanoscale* **2013**, *5*, 9677–9683.

- (17) Zhao, Y.; Luo, X.; Li, H.; Zhang, J.; Araujo, P. T.; Gan, C. K.; Wu, J.; Zhang, H.; Quek, S. Y.; Dresselhaus, M. S.; Xiong, Q. Interlayer Breathing and Shear Modes in Few-Trilayer MoS<sub>2</sub> and WSe<sub>2</sub>. *Nano Lett.* **2013**, *13*, 1007–1015.

- (18) del Corro, E.; Terrones, H.; Elias, A.; Fantini, C.; Feng, S.; Nguyen, M. A.; Mallouk, T. E.; Terrones, M.; Pimenta, M. A. Excited Excitonic States in 1L, 2L, 3L, and Bulk WSe<sub>2</sub> Observed by Resonant Raman Spectroscopy. *ACS Nano* **2014**, *8*, 9629–9635.

- (19) Kaasbjerg, K.; Thygesen, K. S.; Jacobsen, K. W. Phonon-Limited Mobility in N-Type Single-Layer MoS<sub>2</sub> from First Principles. *Phys. Rev. B: Condens. Matter Mater. Phys.* **2012**, *85*, 115317.

- (20) Lee, J.-U.; Park, J.; Son, Y.-W.; Cheong, H. Anomalous Excitonic Resonance Raman Effects in Few-Layered MoS<sub>2</sub>. *Nanoscale* **2015**, *7*, 3229–3236.

- (21) Scheuschner, N.; Gillen, R.; Staiger, M.; Maultzsch, J. Interlayer Resonant Raman Modes in Few-Layer MoS<sub>2</sub>. *Phys. Rev. B: Condens. Matter Mater. Phys.* **2015**, *91*, 235409.

- (22) Chakraborty, B.; Matte, H.; Sood, A.; Rao, C. Layer-Dependent Resonant Raman Scattering of a Few Layer MoS<sub>2</sub>. *J. Raman Spectrosc.* **2013**, *44*, 92–96.

- (23) Fan, J.-H.; Gao, P.; Zhang, A.-M.; Zhu, B.-R.; Zeng, H.-L.; Cui, X.-D.; He, R.; Zhang, Q.-M. Resonance Raman Scattering in Bulk 2H-MX<sub>2</sub> (M = Mo, W; X = S, Se) and Monolayer MoS<sub>2</sub>. *J. Appl. Phys.* **2014**, *115*, 053527.

- (24) Gołasa, K.; Grzeszczyk, M.; Leszczyński, P.; Faugeras, C.; Nicolet, A.; Wysmolek, A.; Potemski, M.; Babiński, A. Multiphonon Resonant Raman Scattering in MoS<sub>2</sub>. *Appl. Phys. Lett.* **2014**, *104*, 092106.

- (25) Guo, H.; Yang, T.; Yamamoto, M.; Zhou, L.; Ishikawa, R.; Ueno, K.; Tsukagoshi, K.; Zhang, Z.; Dresselhaus, M. S.; Saito, R. Double Resonance Raman Modes in Monolayer and Few-Layer  $\text{MoTe}_2$ . *Phys. Rev. B: Condens. Matter Mater. Phys.* **2015**, *91*, 205415.
- (26) Yan, Y. X.; Gamble, E. B., Jr; Nelson, K. A. Impulsive Stimulated Scattering: General Importance in Femtosecond Laser Pulse Interactions with Matter, and Spectroscopic Applications. *J. Chem. Phys.* **1985**, *83*, 5391–5399.
- (27) Cho, G.; Kütt, W.; Kurz, H. Subpicosecond Time-Resolved Coherent-Phonon Oscillations in GaAs. *Phys. Rev. Lett.* **1990**, *65*, 764.
- (28) Cheng, T.; Vidal, J.; Zeiger, H.; Dresselhaus, G.; Dresselhaus, M.; Ippen, E. Mechanism for Displacive Excitation of Coherent Phonons in Sb, Bi, Te, and  $\text{Ti}_2\text{O}_3$ . *Appl. Phys. Lett.* **1991**, *59*, 1923–1925.
- (29) Yee, K.; Lee, K.; Oh, E.; Kim, D.; Lim, Y. Coherent Optical Phonon Oscillations in Bulk GaN Excited by Far Below the Band Gap Photons. *Phys. Rev. Lett.* **2002**, *88*, 105501.
- (30) Cheiwchanchamnangij, T.; Lambrecht, W. R. Quasiparticle Band Structure Calculation of Monolayer, Bilayer, and Bulk  $\text{MoS}_2$ . *Phys. Rev. B: Condens. Matter Mater. Phys.* **2012**, *85*, 205302.
- (31) Zhao, W.; Ribeiro, R. M.; Toh, M.; Carvalho, A.; Kloc, C.; Castro Neto, A. H.; Eda, G. Origin of Indirect Optical Transitions in Few-Layer  $\text{MoS}_2$ ,  $\text{WS}_2$ , and  $\text{WSe}_2$ . *Nano Lett.* **2013**, *13*, 5627–5634.
- (32) Cui, Q.; Ceballos, F.; Kumar, N.; Zhao, H. Transient Absorption Microscopy of Monolayer and Bulk  $\text{WSe}_2$ . *ACS Nano* **2014**, *8*, 2970–2976.
- (33) Nie, Z.; Long, R.; Sun, L.; Huang, C.-C.; Zhang, J.; Xiong, Q.; Hewak, D. W.; Shen, Z.; Prezhdo, O. V.; Loh, Z.-H. Ultrafast Carrier Thermalization and Cooling Dynamics in Few-Layer  $\text{MoS}_2$ . *ACS Nano* **2014**, *8*, 10931–10940.
- (34) Pöllmann, C.; Steinleitner, P.; Leierseder, U.; Nagler, P.; Plechinger, G.; Porer, M.; Bratschitsch, R.; Schüller, C.; Korn, T.; Huber, R. Resonant Internal Quantum Transitions and Femtosecond Radiative Decay of Excitons in Monolayer  $\text{WSe}_2$ . *Nat. Mater.* **2015**, *14*, 889–893.
- (35) Yan, T.; Qiao, X.; Liu, X.; Tan, P.; Zhang, X. Photoluminescence Properties and Exciton Dynamics in Monolayer  $\text{WSe}_2$ . *Appl. Phys. Lett.* **2014**, *105*, 101901.
- (36) Zhu, C.; Zhang, K.; Glazov, M.; Urbaszek, B.; Amand, T.; Ji, Z.; Liu, B.; Marie, X. Exciton Valley Dynamics Probed by Kerr Rotation in  $\text{WSe}_2$  Monolayers. *Phys. Rev. B: Condens. Matter Mater. Phys.* **2014**, *90*, 161302.
- (37) Moody, G.; Dass, C. K.; Hao, K.; Chen, C.-H.; Li, L.-J.; Singh, A.; Tran, K.; Clark, G.; Xu, X.; Berghäuser, G.; Malic, E.; Knorr, A.; Li, X. Intrinsic Homogeneous Linewidth and Broadening Mechanisms of Excitons in Monolayer Transition Metal Dichalcogenides. *Nat. Commun.* **2015**, *6*, 8315.
- (38) Terrones, H.; Del Corro, E.; Feng, S.; Poumirol, J.; Rhodes, D.; Smirnov, D.; Pradhan, N.; Lin, Z.; Nguyen, M.; Elias, A.; Mallouk, T. E.; Balicas, L.; Pimenta, M. A.; Terrones, M. New First Order Raman-Active Modes in Few Layered Transition Metal Dichalcogenides. *Sci. Rep.* **2014**, *4*, 4215.
- (39) Gupta, A.; Chen, G.; Joshi, P.; Tadigadapa, S.; Eklund, P. Raman Scattering from High-Frequency Phonons in Supported N-Graphene Layer Films. *Nano Lett.* **2006**, *6*, 2667–2673.
- (40) Ferrari, A. C. Raman Spectroscopy of Graphene and Graphite: Disorder, Electron–Phonon Coupling, Doping and Nonadiabatic Effects. *Solid State Commun.* **2007**, *143*, 47–57.
- (41) Ge, S.; Liu, X.; Qiao, X.; Wang, Q.; Xu, Z.; Qiu, J.; Tan, P.-H.; Zhao, J.; Sun, D. Coherent Longitudinal Acoustic Phonon Approaching THz Frequency in Multilayer Molybdenum Disulphide. *Sci. Rep.* **2014**, *4*, 5722.
- (42) Menéndez, J.; Cardona, M. Temperature Dependence of the First-Order Raman Scattering by Phonons in Si, Ge, and  $\alpha$ -Sn: Anharmonic Effects. *Phys. Rev. B: Condens. Matter Mater. Phys.* **1984**, *29*, 2051.
- (43) Kresse, G.; Joubert, D. From Ultrasoft Pseudopotentials to the Projector Augmented-Wave Method. *Phys. Rev. B: Condens. Matter Mater. Phys.* **1999**, *59*, 1758.
- (44) Tkatchenko, A.; Scheffler, M. Accurate Molecular van der Waals Interactions from Ground-State Electron Density and Free-Atom Reference Data. *Phys. Rev. Lett.* **2009**, *102*, 073005.
- (45) Debbichi, L.; Eriksson, L. O.; Lebègue, S. Electronic Structure of Two-Dimensional Transition Metal Dichalcogenide Bilayers from Ab Initio Theory. *Phys. Rev. B: Condens. Matter Mater. Phys.* **2014**, *89*, 205311.
- (46) Ramasubramaniam, A. Large Excitonic Effects in Molybdenum and Tungsten Dichalcogenides. *Phys. Rev. B: Condens. Matter Mater. Phys.* **2012**, *86*, 115409.